

UC Santa Cruz

UC Santa Cruz Previously Published Works

Title

Photoinduced structural recovery dynamics of rare-earth nickelate thin films

Permalink

<https://escholarship.org/uc/item/8z62121k>

Journal

Physical Review Materials, 7(9)

ISSN

2476-0455

Authors

Mehta, Jugal
Smith, Scott
Li, Jianheng
[et al.](#)

Publication Date










2023-09-01

DOI

10.1103/physrevmaterials.7.096201

Peer reviewed

Photoinduced structural recovery dynamics of rare-earth nickelate thin films

Jugal Mehta ¹, Scott Smith ¹, Jianheng Li,¹ Kenneth Ainslie,¹ Nadia Albayati,¹ Toyanath Joshi,² Pooja Rao ¹, Yu-Hsing Cheng ¹, Spencer Jeppson ¹, Rahul Jangid ¹, Evguenia Karapetrova,³ Donald A. Walko,³ Haidan Wen ^{3,4}, David Lederman ² and Roopali Kukreja ^{1,*}

¹Department of Materials Science and Engineering, University of California Davis, Davis, California 95616, USA

²Department of Physics, University of California Santa Cruz, Santa Cruz, California 95064, USA

³Advanced Photon Source, Argonne National Laboratory, Lemont, Illinois 60439, USA

⁴Materials Science Division, Argonne National Laboratory, Lemont, Illinois 60439, USA



(Received 3 January 2023; revised 14 June 2023; accepted 14 August 2023; published 7 September 2023)

Photoinduced structural dynamics of rare-earth nickelate thin films, NdNiO₃ and SmNiO₃, grown on (001) oriented SrTiO₃ were studied using time-resolved x-ray diffraction. The evolution of the (002) Bragg peak was tracked following laser excitation. The recovery pathways were found to be strongly dependent on laser fluence for NdNiO₃ and distinct for the two rare-earth nickelates. The recovery of the (002) peak shifts was modeled using a one-dimensional thermal diffusion model which showed that the recovery processes are nonthermal at high fluences. For NdNiO₃, the timescales for the recovery of the (002) peak shift were found to be closely related to Ni magnetism recovery, potentially indicating magnetostructural coupling. Moreover, the evolution of integrated intensity and full width at half maximum points towards the presence of a structural phase separation during recovery. Our studies highlight structural recovery pathways in nickelates by comparing the distinct responses of the photoinduced metal-insulator transition in NdNiO₃ and SmNiO₃.

DOI: [10.1103/PhysRevMaterials.7.096201](https://doi.org/10.1103/PhysRevMaterials.7.096201)

I. INTRODUCTION

Photoexcitation by means of ultrashort optical laser pulses provides a powerful approach to initiate and manipulate an insulator-to-metal transition (IMT) in transition metal oxides [1–5]. In comparison to other methods of controlling IMT such as epitaxial strain [6,7], doping [8,9], magnetic field [10,11], or applied voltage [12,13], photoexcitation provides a unique way to identify the interplay of electronic, magnetic, and structural degrees of freedom in time domain. It also enables access to transient metastable states not observed in thermal equilibrium [14]. Recently, it has been shown that the photoinduced IMT in rare-earth nickelates (RNiO₃ where R = Nd, Pr, Sm, Eu, etc.) can be driven at subpicosecond timescales with a laser fluence nearly an order of magnitude smaller than the widely studied vanadate system [15,16]. Additionally, the IMT can be tuned to near room temperature via substrate strain [6], substrate symmetry [17], or by choice of rare-earth cation [18], making rare-earth nickelates excellent candidates for ultrafast manipulation.

RNiO₃ undergoes a metal-to-insulator transition (MIT) on cooling during which the crystal structure transforms from orthorhombic (P_{bmm}) to monoclinic ($P_{2_1/c}$), the paramagnetic state switches to an antiferromagnetic state, and charge ordering occurs [18–20]. In RNiO₃, the magnetic and electronic properties can be tuned by varying the tolerance factor of the perovskite structure. A smaller rare-earth cation leads to a more distorted structure, resulting in a 500-K variation of

the transition temperature (T_{MIT}) as the rare-earth cation size decreases from Pr to Lu for bulk nickelates [18]. For NdNiO₃ (NNO), the T_{MIT} and Neel temperature (T_N) coincide while nickelates with smaller rare-earth cations such as SmNiO₃ (SNO) show a separation of the electronic and magnetic transition with $T_{MIT} > T_N$. Heteroepitaxial strain results in separation of the insulator-to-metal and the magnetic phase transition temperature observed in bulk NNO, and compressive strain can lead to disappearance of the MIT, resulting in metallic films over the entire temperature range [6]. As epitaxial strain or rare-earth cation can significantly alter the phase diagram, photoinduced measurements of the nickelate family can provide unique insights into the coupling of electronic, magnetic, and structural degrees of freedom as well as methods to tailor ultrafast behavior.

In this article, we have utilized time-resolved x-ray diffraction (tr-XRD) to study the photoinduced structural recovery dynamics of tensile strained NNO and SNO thin films. While extensive work has been performed on understanding excitation pathways from the insulating to the metallic state [16,21–29], only a few studies have focused on the recovery pathways from the metallic to insulating state in nickelates [15]. Our tr-XRD experiments for NNO revealed a strong laser fluence dependence for structural recovery, indicating the presence of nonthermal pathways at higher fluence. The sign of Bragg peak shifts for both NNO and SNO is consistent with thermal diffusion model calculations. Photoinduced strain recovery in NNO occurs at similar timescales as Ni magnetism [26], indicating magnetostructural pathways for recovery. Measurement of the full width at half maximum and integrated intensity of the (002) Bragg peak suggests structural phase

*Corresponding author: rkukreja@ucdavis.edu

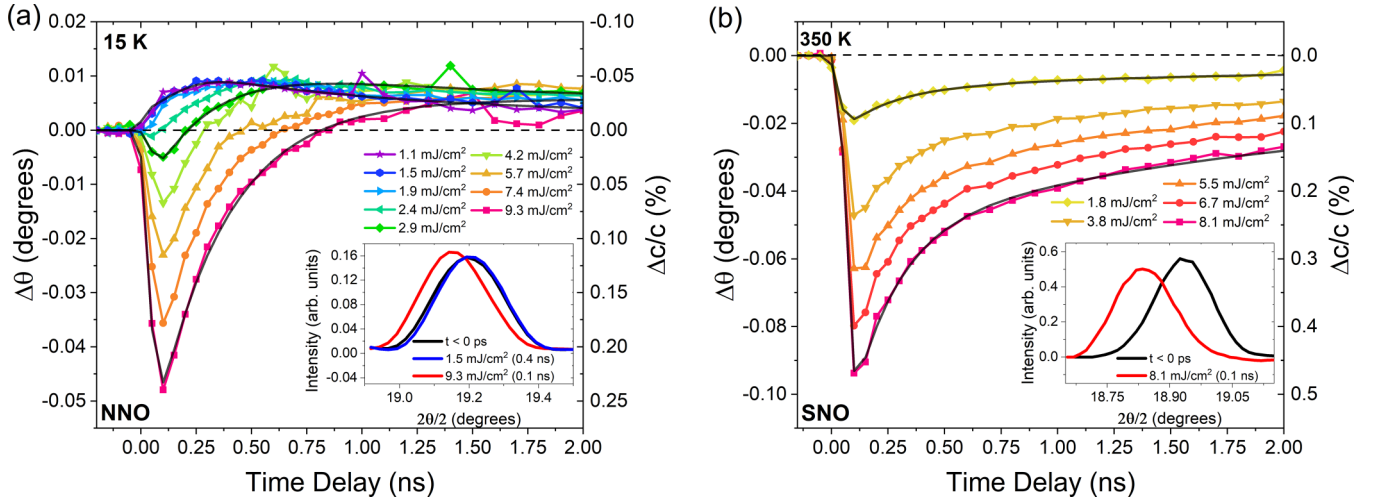


FIG. 1. Photoinduced structural evolution of NNO and SNO thin films: (a) NNO (002) peak shift as a function of time delay for different incident pump fluences. The inset shows NNO (002) Bragg peak at 100 ps after photoexcitation for a fluence of 9.3 mJ/cm² (red) and 400 ps for a fluence of 1.5 mJ/cm² (blue), and the Bragg peak before laser excitation (black). For the low fluence, the peak shift indicates a lattice contraction which reaches its maximum value at 400 ps, while for the higher fluence, the peak shift shows a lattice expansion which reaches its maximum value at 100 ps. (b) SNO (002) peak shift as a function of time delay for different incident pump fluences. The inset shows SNO (002) Bragg peak before photoexcitation (black) and at 100 ps for a laser fluence of 8.1 mJ/cm² (red). The SNO peak shift shows an out-of-plane expansion of the lattice within 100 ps. Black lines overlaid on the delay curves represent exponential fits as described in the text.

separation, which is consistent with recent reports for NNO [15]. Phase separation is not observed for SNO, highlighting the distinct response of two nickelates with different rare-earth cations. The coupling of structural recovery with magnetism as well as domain dynamics at ultrafast timescales reveals the rich transient physics observed in rare-earth nickelates.

II. EXPERIMENTAL METHODS

A NNO thin film (19 nm) was deposited on a (001) oriented SrTiO₃ (STO) substrate using rf magnetron sputtering in a 3:1 Ar/O₂ environment and a total pressure of 130 mTorr at 500 °C. A SNO thin film (30 nm) was deposited on a (001) oriented STO substrate using pulsed laser deposition [30]. Reciprocal space maps around the (103) peaks confirmed that both films are commensurate with the substrate. Note that pseudocubic notation is used throughout the article for Miller indices. The STO substrate imparts a heteroepitaxial tensile strain of 2.6% and 2.7% for the NNO and SNO film, respectively. $\theta - 2\theta$ scans of the (002) Bragg peak show that the out-of-plane lattice parameter of NNO and SNO thin films is 3.778 Å and 3.816 Å at 300 K, respectively. Resistivity measurements indicate T_{MIT} of 106 K for NNO and above 400 K for SNO (see Sec. S1 of the Supplemental Material [31]). The variation in T_{MIT} of these films compared to literature could be due to oxygen deficiencies caused by high tensile strain. The temperature-dependent x-ray diffraction (XRD) data on NNO and SNO were collected at Sector 33 at the Advanced Photon Source (APS) with an x-ray energy of 16 keV and will be discussed below in Sec. IV.

Tr-XRD measurements were performed at Sector 7 at APS at Argonne National Laboratory. Laser pulses with 60-fs pulse width (“pump”) from a Ti:sapphire laser system (repetition

rate 1 kHz) were used to induce the IMT. The pump wavelength (800 nm) is above the band gap of NNO and SNO. The laser fluences are reported in terms of the incident fluence. The photoinduced structural changes were measured using x-ray pulses tuned to 10 keV (“probe”). The x-ray spot size was 50 μm and 100 μm for NNO and SNO, respectively, and the laser spot size was 500 μm. Tr-XRD measurements were performed at (002) and $(\frac{1}{2}\frac{1}{2}\frac{3}{2})$ Bragg peaks for a delay range of -0.2–6 ns for NNO and -0.15–10 ns for SNO. Diffracted x-ray photons were collected by a two-dimensional pixel array detector (Pilatus 100K, Dectris Ltd.) with a pixel size of 172 μm. $\theta - 2\theta$ scans of the (002) Bragg peak and L-scans of the $(\frac{1}{2}\frac{1}{2}\frac{3}{2})$ taken at specific time delays after laser excitation were fit with a Gaussian curve to extract peak position and full width at half maximum (FWHM) of the peak. The area under the curve was calculated to obtain the integrated intensity. Note that the presence of twinned orthorhombic domains in NNO/STO films can also contribute to the intensity of the half-order Bragg peak [36]. Photoinduced changes in these parameters are plotted relative to the before-time zero value throughout the article.

III. EXPERIMENTAL RESULTS

Figure 1 shows the (002) peak shift ($\Delta\theta$) for NNO and SNO films following photoexcitation for a range of pump laser fluences. NNO was photoexcited from its antiferromagnetic insulating phase at 15 K, whereas SNO was photoexcited from its paramagnetic insulating phase at 350 K. A clear sign reversal of the photoinduced peak shift with increasing laser fluence is observed for NNO in Fig. 1(a). For 1.1–1.9 mJ/cm², a positive $\Delta\theta$ indicating a decrease in the c-lattice parameter is observed, while above 2.4 mJ/cm², a negative $\Delta\theta$ indicating

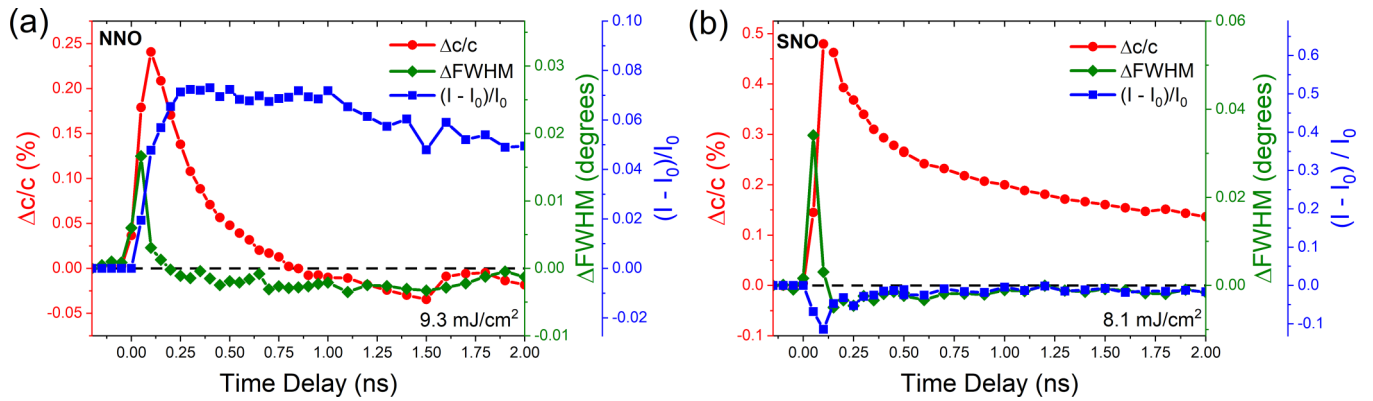


FIG. 2. Comparison of photoinduced strain (red circles), FWHM (green diamonds), and integrated intensity (blue squares) for (002) Bragg peak for (a) NNO film for a pump fluence of 9.3 mJ/cm² and (b) SNO film for a pump fluence of 8.1 mJ/cm².

an increase in the *c*-lattice parameter is measured. The inset in Fig. 1(a) shows NNO (002) Bragg peak for pump fluence of 1.5 mJ/cm² at 400 ps and 9.3 mJ/cm² at 100 ps. The comparison with Bragg peak before photoexcitation clearly shows the shift in opposite directions for the two pump fluences. For SNO, all fluences result in a photoinduced peak shift towards lower theta values, indicating expansion along the *c* axis as shown in Fig. 1(b). The inset in Fig. 1(b) shows the SNO (002) Bragg peak for a pump fluence of 8.1 mJ/cm² at 100 ps.

The photoinduced evolution of the (002) Bragg peak was fit using an exponential function as described in Sec. S3 of the Supplemental Material (SM) [31]. The results of the temporal fits are shown in Figs. 1(a) and 1(b) (black curves) and time constants are tabulated in Table S1 in the SM [31]. For NNO, the peak shift dynamics can be separated into three fluence regimes: low, intermediate, and high. In the low fluence regime (1.1–1.9 mJ/cm²), the laser excitation leads to a positive $\Delta\theta$ (τ_1) which reaches a maximum value within 400 ps, after which it starts to recover (τ_2). The time constants $\tau_1 \sim 150$ ps and $\tau_2 \sim 1$ –2 ns are similar for all fluences in the low fluence regime. In the intermediate fluence regime (2.4–4.2 mJ/cm²), the laser excitation leads to a negative $\Delta\theta$ within <100 ps, limited by the temporal resolution of the experiment. An initial quick recovery ($\tau_1 \sim 200$ ps) results in $\Delta\theta$ crossing zero and becoming positive, followed by a longer recovery ($\tau_2 \sim 1$ –2 ns). For the high fluence regime (5.7–9.3 mJ/cm²), an immediate negative $\Delta\theta$ (< 100 ps) succeeded by a quick recovery (τ_1) which results in overshooting the initial ground state, followed by a slow recovery, is observed. For the high fluence regime, τ_1 shows a fluence dependence and increases from 240 ps \pm 20 ps to 320 ps \pm 20 ps for 5.7–9.3 mJ/cm². Following the initial quick recovery, the value of $\Delta\theta$ remains almost constant within the measured range of 6 ns, indicating a longer recovery compared to intermediate and low fluences. In comparison, the photoinduced evolution for SNO varies monotonically with the increasing laser fluence with no distinct fluence regimes. As shown in Fig. 1(b) for SNO, an immediate negative $\Delta\theta$ is observed within 100 ps and the recovery process consists of a quick recovery ($\tau_1 \sim 200$ ps) and a slow recovery ($\tau_2 \sim 2$ ns) for all the measured fluences.

In order to further investigate the photoinduced structural recovery, the (002) Bragg peak was fit with a Gaussian profile

to obtain integrated intensity and FWHM, which are related to changes in crystal symmetry and crystallite size, respectively. Figure 2 compares the temporal evolution of out-of-plane strain, FWHM, and integrated intensity for (002) Bragg peak for the highest fluence measured for both NNO and SNO thin films (other fluences are presented in Sec. S4 of the SM [31]). A clear difference between temporal evolution of strain, FWHM, and integrated intensity is observed for both thin films, indicating the presence of multiple processes during recovery. For NNO, the FWHM achieves a maximum value at ~ 50 ps, whereas the strain shows a maximum at ~ 100 ps. While the 50–100-ps pulse width of synchrotron x-rays limits insight into this decoupling during excitation, it provides information regarding recovery processes. The FWHM overshoots the initial value during the quick recovery, resulting in a sign reversal which recovers slowly to the initial state. On the other hand, the integrated intensity shows a continuous increase followed by a slower decay to the initial state. For SNO, both the FWHM and integrated intensity show a different temporal evolution compared to NNO. After laser excitation, fast modification is observed for both FWHM and integrated intensity, which recovers within ~ 250 ps to the initial state.

We also measured the half-order peak ($\frac{1}{2}\frac{1}{2}\frac{3}{2}$) for NNO and ($\frac{1}{2}\frac{1}{2}\frac{3}{2}$) for SNO (Secs. S5 and S6 of the SM [31], respectively.), which arises due to octahedral rotations in the perovskite structure [37]. Similar to the (002) peak, a shift to higher *L* is observed for low fluences for the NNO half order peak, whereas high fluences cause a shift to lower *L*. On the other hand, no photoinduced change in peak position, FWHM, or integrated intensity was observed in the *h* direction, indicating that epitaxial strain from the substrate effectively pins the in-plane lattice parameters of the film.

Figure 3 shows the fluence dependence for strain, FWHM, and integrated intensity of the (002) Bragg peak. The comparison of photoinduced strain for NNO and SNO thin films at 100 ps clearly shows nonlinear and linear fluence dependence, respectively. The sign reversal in strain for NNO is similar to temperature-dependent static XRD, which will be discussed in Sec. IV. Figure 4(b) presents an average FWHM value for a time delay range of 1 ns \pm 0.25 ns. For NNO, no significant change in FWHM is observed for the low and intermediate fluence regime, whereas a decrease in the FWHM is seen in

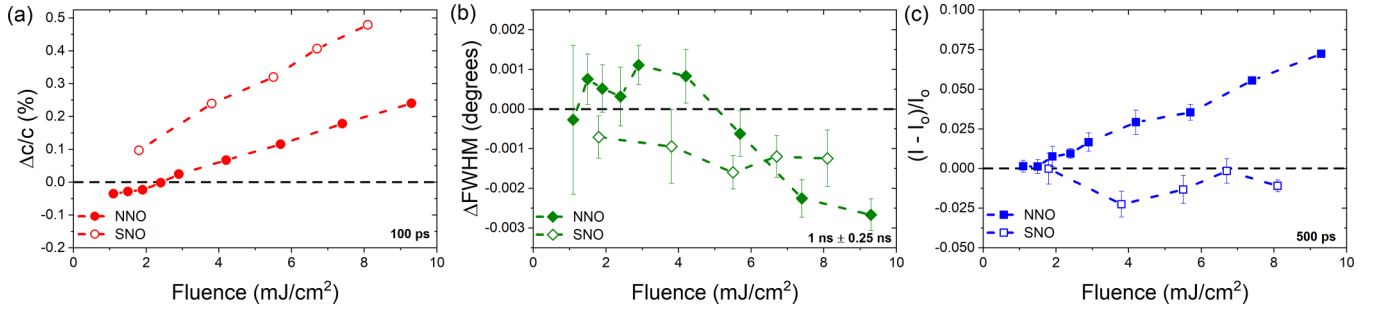


FIG. 3. Fluence dependence of strain, FWHM, and integrated intensity: (a) Photoinduced changes in out-of-plane strain of NNO (closed red circles) and SNO (open red circles) at 100 ps as a function of laser fluence. Error bars are on the order of symbol size for strain. (b) Photoinduced change in (002) FWHM of NNO (closed green diamonds) and SNO (open green diamonds) as a function of laser fluence. An average of FWHM in the time delay range of 0.75–1.25 ns is shown with error bars representing standard deviation. (c) Photoinduced change in (002) integrated intensity of NNO (closed blue squares) and SNO (open blue squares) at 500 ps as a function of laser fluence. Error bars represent standard deviation of integrated intensity before laser excitation.

the high fluence regime. For SNO, no fluence dependence of FWHM is detected. Figure 3(c) plots the integrated intensity at 500 ps for NNO and SNO. For NNO, no significant change is observed for the low fluence regime, while a linear fluence dependence is observed for the intermediate and high fluence regime. This linear increase in integrated intensity is higher than the calculated increase of 0.01% due to a change in crystal symmetry from monoclinic ($P2_1/n$) to orthorhombic ($Pbnm$) crystal structure using atomic positions reported in Garcia-Munoz *et al.* [20]. In contrast, no significant change in integrated intensity is observed for SNO. The striking differences in fluence dependence of NNO and SNO indicate different recovery processes at play for the two nickelate systems. Thermal modeling and analysis was performed to further discern the recovery processes underlying the structural evolution in nickelate thin films.

IV. THERMAL MODEL AND ANALYSIS

A one-dimensional thermal diffusion equation of a heterostructure was solved numerically to generate a film temperature vs time profile (Sec. S8 of the SM [31]). A similar model has been previously utilized for complex oxide thin-film heterostructures [38,39]. While most sample parameters used in the model were obtained from literature, interface conductance, an important parameter in determining the cooling rate estimated by the thermal model, is not currently available for NNO/STO and SNO/STO. Thermal simulations were carried out for 1 000 $\text{W}/\text{cm}^2 \text{ K}$ and 100 000 $\text{W}/\text{cm}^2 \text{ K}$ to cover a range of values typically seen for oxides. For example, the $\text{SrRuO}_3/\text{SrTiO}_3$ heterostructure has one of the highest reported values of interface conductance of 80 000 $\text{W}/\text{cm}^2 \text{ K}$ [40]. A higher interface conductivity value of 100 000 $\text{W}/\text{cm}^2 \text{ K}$ resulted in a better fit of experimental data at lower and intermediate fluences (Fig. S12 of SM), and thus was used for the simulations.

The temperature vs time curves obtained from the thermal diffusion model were converted to $\Delta\theta$ vs time delay by utilizing temperature-dependent XRD data measured in thermal equilibrium. However, one important caveat is that during laser excitation the substrate remains near the ambient temperature (pump energy is below the band gap of STO),

while in temperature-dependent XRD measurements both the substrate and film are in thermal equilibrium. In order to address this difference, we modified the temperature-dependent XRD curve to include Poisson's expansion due to in-plane clamping of the film by the substrate (Sec. S8 of the Supplemental Material [31]). Figures 4(a) and 4(b) present the (002) peak shift of NNO and SNO, respectively, obtained using temperature-dependent XRD measurements, as well as a peak shift calculated after considering the in-plane epitaxial constraint imparted by the substrate. Note that peak shifts $\Delta\theta$ are plotted relative to the (002) peak position at 30 K for NNO and 350 K for SNO. The measured XRD for NNO (black curve) shows that as the film is heated from its insulating state, $\Delta\theta$ increases until T_{IMT} is achieved, after which $\Delta\theta$ starts to decrease again, indicating contraction followed by expansion of the unit cell. This is consistent with the literature for films grown on STO [36]. The substrate constraint calculated peak shift (blue curve) also shows similar behavior, albeit with larger magnitude due to in-plane epitaxial constraint. Considering substrate constraint for SNO leads to a larger negative $\Delta\theta$, i.e., expansion of the c-lattice parameter which increases with temperature. Note that while the temperature dependence of the lattice parameter for SNO thin films has not been reported in the literature, the c-lattice parameter of bulk SNO shows a change at the T_{MIT} similar to NNO. For films, the tensile in-plane strain from the substrate or the presence of oxygen vacancies could be responsible for differences in behavior compared to bulk.

Figures 4(c)–4(f) compare the simulated peak shifts ($\Delta\theta_{\text{thermal}}$) with experimental peak shifts ($\Delta\theta_{\text{experiment}}$) for NNO and SNO. Note that $\Delta\theta_{\text{thermal}}$ and $\Delta\theta_{\text{experiment}}$ have been normalized for comparison. For the low and intermediate fluences, normalization was done using the maxima in the peak shift while for higher fluences and SNO, normalization was done using minima in the peak shift. Three key observations can be made from the calculated temperatures and simulated peak shifts for NNO. Firstly, the lowest measured fluence of 1.1 mJ/cm^2 leads to a film temperature of 161 K, implying that laser excitation can drive the IMT even for the low fluence regime. The corresponding temperature for a given fluence is indicated in Fig. 4(a). Secondly, the sign of an experimentally observed peak shift for all fluences is

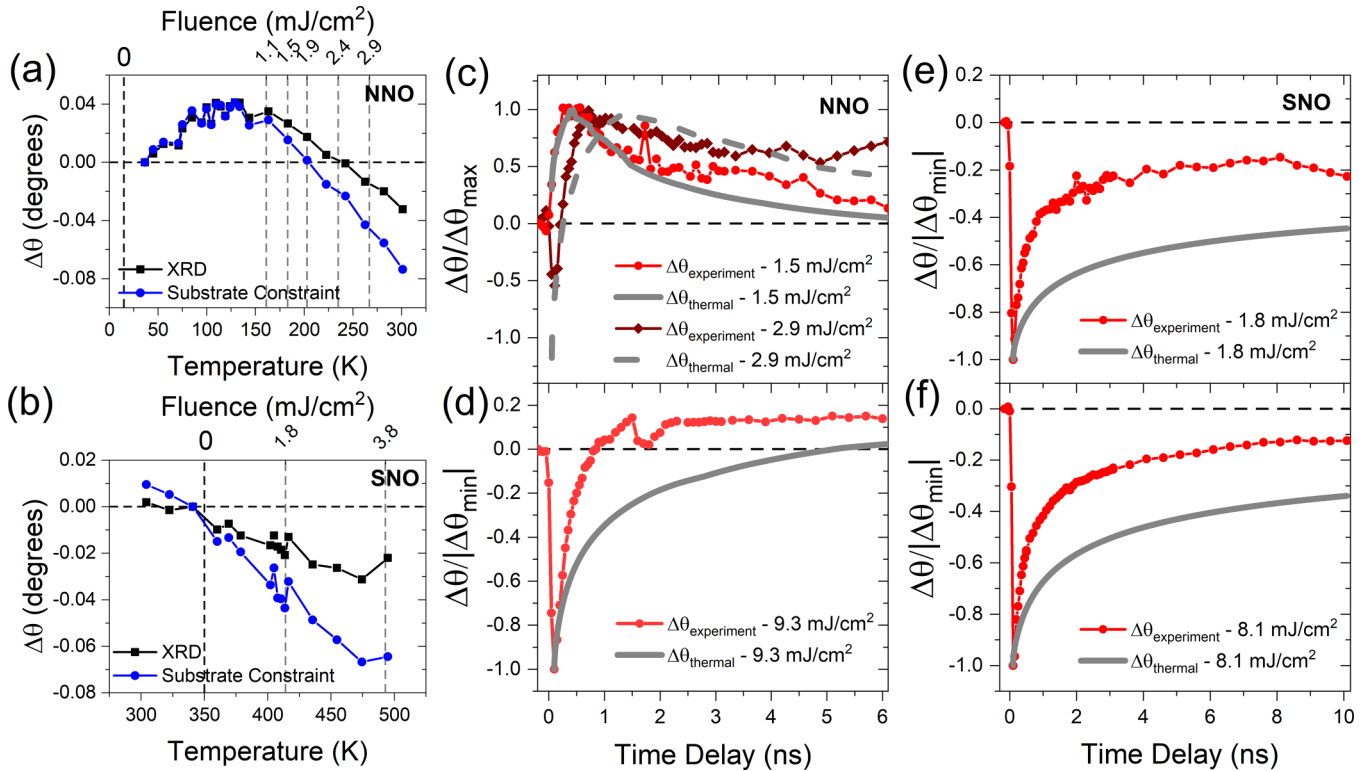


FIG. 4. Thermal diffusion modeling of NNO and SNO: Temperature dependence of (002) peak shift for (a) NNO and (b) SNO obtained from temperature-dependent XRD measurements (black squares) and after including in-plane clamping by substrate (blue circles). Vertical dashed lines mark the initial film temperature achieved for respective pump fluence. Comparison of experimental and simulated NNO (002) peaks shift for pump fluence of (c) 1.5 mJ/cm² (circles) and 2.9 mJ/cm² (diamonds) and (d) 9.3 mJ/cm². Comparison of experimental and simulated SNO (002) peak shift for pump fluence of (e) 1.8 mJ/cm² and (f) 8.1 mJ/cm². Simulations were done for an interface conductance of 100 000 W/cm² K and assuming an initial sample temperature of 15 K and 350 K for NNO and SNO, respectively, the same as the experimental measurements.

reproduced by the model. Specifically, the thermal diffusion model and simulated peak shift can explain the photoinduced peak shift for low and intermediate fluences. As the film temperature is only slightly above T_{IMT} for the low fluence regime, a positive photoinduced peak shift is observed for both experimental and simulated curves. During recovery as the temperature lowers, a maxima in $\Delta\theta$ is observed due to the inverted U-shape of temperature-dependent XRD [Fig. 4(a)]. Increasing the fluence to the intermediate regime leads to higher temperature, which corresponds to negative $\Delta\theta$, consistent with temperature dependent XRD. During recovery, as the film temperature lowers, $\Delta\theta$ traverses temperature-dependent XRD, which results in a sign reversal and a maxima in the peak shift again due to the inverted U-shape of the XRD. Note that the maxima in peak shift is the same for low and intermediate fluence regimes as the film reaches same structure dictated by temperature-dependent XRD. Lastly, for the high fluence regime, the simulated peak shift cannot reproduce experimentally observed behavior. However, the model correctly shows that the film does not cool fast enough to traverse the inverted U shape of temperature-dependent XRD within the measured delay range, which is consistent with the experimental observation of no maxima observed in peak shift for the high fluence regime. The disparity be-

tween recovery timescales estimated by the thermal diffusion model and experiment increases with increasing laser fluence points towards nonthermal recovery behavior at higher fluences.

For SNO, experimentally observed negative peak shifts are consistent with simulated peak shifts. However, the simulated recovery rates of $\Delta\theta_{thermal}$ are slower than experimentally observed peak shifts $\Delta\theta_{experiment}$ even at lower fluences. The discrepancy between $\Delta\theta_{thermal}$ and $\Delta\theta_{experiment}$ could be due to additional factors not included in this simple model. For example, due to a lack of material parameters for SNO such as band gap and thermal conductivity, parameters of NNO were used. Furthermore, a Poisson ratio of 0.3 was assumed for the calculations. Additionally, an assumption that heat capacity for bulk can be used for thin films can also potentially introduce errors in temperature estimates. Overestimation of temperature can also occur due to the absence of a latent heat term in the model. Additionally, limited temperature range of thermal XRD measurements implies that linear extrapolation was used to estimate peak shift at higher temperatures, which can overestimate the calculated peak shifts. Overall, these simulations suggest that while the sign of photoinduced structural changes seen in NNO and SNO is dictated by thermal transport, the role of nonthermal processes for high

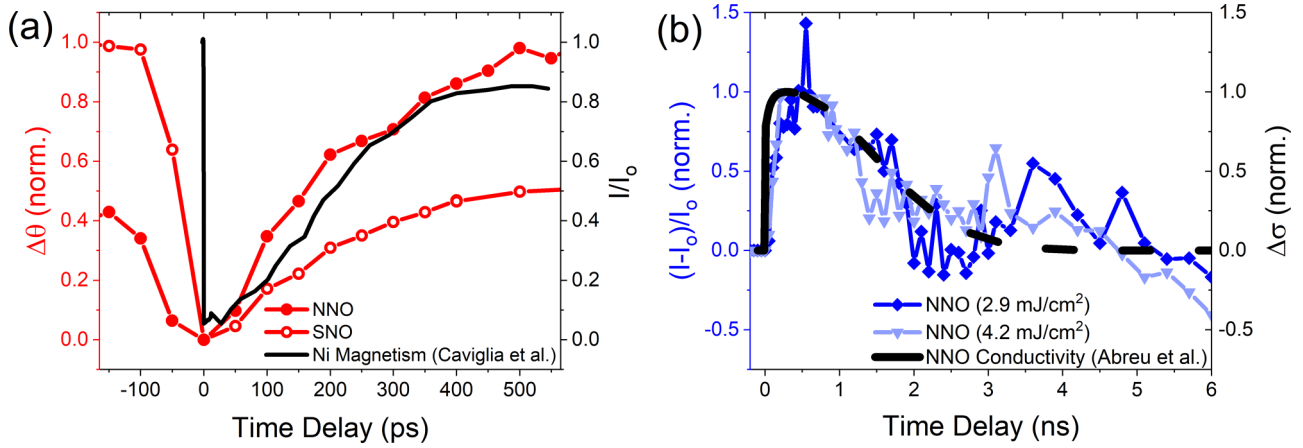


FIG. 5. Comparison of photoinduced recovery of structural (this article), magnetic [26], and electronic degrees of freedom [15]: (a) Comparison of the (002) peak shift for NNO and SNO observed in our study with Ni magnetism dynamics reported by Caviglia *et al.* [26] for NNO. Black curve represents Ni magnetism following photoexcitation of NNO from 40 K with a laser fluence of 2.7 mJ/cm², which is compared with the (002) peak shift of NNO from 15 K (closed red circles) and SNO from 350 K (open red circles) with a laser fluence of 2.9 mJ/cm² and 3.8 mJ/cm², respectively. (b) Comparison of NNO (002) integrated intensity with the ultrafast THz conductivity dynamics of NNO reported by Abreu *et al.* [15]. The black curve represents the THz conductivity of NNO measured at 103 K following photoexcitation with laser fluence of 1.5 mJ/cm², which is compared with the change in integrated intensity for NNO measured at 15 K with a laser fluence of 2.9 mJ/cm² (blue diamonds) and 4.2 mJ/cm² (light blue inverted triangles). Dashed black lines for conductivity are generated from the equation of fit provided in Ref. [15]. Note that curves are normalized to compare recovery timescales.

fluences cannot be ruled out due to limitations of the thermal model.

V. DISCUSSION

As mentioned above, the thermal diffusion model simulates major aspects of the recovery dynamics for low and intermediate fluences for NNO. However, the fast recovery of NNO (002) peak shift for the higher fluence regime cannot be reproduced by the thermal diffusion model. Additionally, in the high fluence regime, the photoinduced increase in integrated intensity of the NNO (002) Bragg peak (Fig. 2 and SM Fig. S4) is higher than expected from structure factor calculations. Both the peak shift and integrated intensity behavior thus point towards nonthermal recovery in the high fluence regime.

We compared the structural dynamics measured in this article with recovery dynamics of magnetism [26] and conductivity [15] in NNO, reported in the literature for the same excitation wavelength (800 nm) and laser fluences that led to comparable film temperatures. Ultrafast resonant soft x-ray magnetic scattering measurements of NNO conducted by Caviglia *et al.* [26] have shown that higher pump fluences (>1 mJ/cm², excited from a temperature of 40 K) lead to a complete quenching of the antiferromagnetic order at the Ni site, which recovers with a time constant >100 ps. Figure 5(a) compares the ultrafast evolution of Ni magnetism and the (002) peak shift for NNO and SNO. We see that the NNO peak shift recovers at similar timescales as that of Ni magnetism, while SNO recovery is slower than NNO and Ni magnetism. Similar recovery timescales for structural Bragg peak and Ni magnetism point towards magnetostructural coupling, which has been reported to play a major role in driving photoinduced IMT in NNO [16]. On the other hand, while the

recovery of SNO peak shift is slower than that of NNO, direct measurements of Ni magnetism dynamics in SNO below Neel temperature are required to conclusively understand the role of magnetism on the photoexcited structural dynamics. Structural measurements at ultrafast timescales (1–100 ps) could provide further insights into coupling of magnetism, electronic, and structural degrees of freedom.

Figure 5(b) compares the evolution of (002) integrated intensity measured in our study with the ultrafast THz conductivity behavior of NNO [15]. The slow nonexponential recovery observed in the THz conductivity dynamics was attributed to nucleation and growth of the insulating domains from the metallic domains as the film cools below T_{MIT} . The striking similarity in the recovery profiles could be due to a similar process at play. This phase separated and heterogeneous excited state can result in strain gradients and mosaicism in the film which can cause integrated intensity variations [41,42]. On the other hand, no such increase in integrated intensity is observed for SNO. While THz conductivity studies of SNO are not yet available in literature, THz conductivity of EuNiO₃, which also has a smaller tolerance factor than NNO and displays a separation in T_{MIT} and T_N similar to SNO, shows an exponential recovery due to the absence of nucleation and growth [15]. The resultant system would have minimal strain gradient and could be a reason for no observed variation in integrated intensity at >250 ps timescales. X-ray microscopy studies at ultrafast timescales would be important to uncover the spatial heterogeneity in nickelates.

VI. CONCLUSION

In summary, we performed a comprehensive study of structural dynamics in rare-earth nickelate thin films as a function

of pump fluences. The photoinduced behavior of the out-of-plane lattice parameter shows a distinct response for NNO and SNO which was explained using a one-dimensional thermal diffusion model. The photoinduced recovery of the out-of-plane lattice parameter occurs at similar timescales as that of ultrafast Ni magnetism, hinting towards magnetostructural coupling at ultrafast timescales. The integrated intensity and FWHM capture indications of a photoinduced phase separation in NNO that is absent for SNO, implying that the first-order nature of MIT of NNO is manifested in ultrafast processes. Overall, the decoupling of recovery timescales for photoinduced strain and integrated intensity points towards a thermally inaccessible structural state with complex recovery pathways where the system is phase separated into metallic and insulating domains, and magnetism is potentially linked to the photoinduced strain. These insights enable understanding of the recovery mechanisms of the lattice and its interactions with multiple degrees of freedom at nanosecond timescales

and nano- to mesolength scales, which can help facilitate faster magnetic and electronic switching.

ACKNOWLEDGMENTS

We thank Prof. Paul Evans and Dr. Sangeeta Rajpurohit for fruitful discussions on temporal dynamics of nickelates. This work was supported by the National Science Foundation (Grant No. DMR-1902652). The work at UC Santa Cruz was partially supported by the Air Force MURI program, Grant No. FA9550-19-1-030. H.W. acknowledges the support for assisting time-resolved X-ray diffraction by the U.S. Department of Energy, Basic Energy Sciences, Materials Sciences and Engineering Division. This research used resources from the Advanced Photon Source, a US Department of Energy (DOE) Office of Science User Facilities operated for the DOE Office of Science by Argonne National Laboratory (under Contract No. DE-AC02-06CH11357).

-
- [1] M. Fiebig, K. Miyano, Y. Tomioka, and Y. Tokura, Visualization of the local insulator-metal transition in $\text{Pr}_{0.7}\text{Ca}_{0.3}\text{MnO}_3$, *Science* **280**, 1925 (1998).
- [2] A. Cavalleri, C. Tóth, C. W. Siders, J. A. Squier, F. Ráksi, P. Forget, and J. C. Kieffer, Femtosecond Structural Dynamics in VO_2 during an Ultrafast Solid-Solid Phase Transition, *Phys. Rev. Lett.* **87**, 237401 (2001).
- [3] A. Tomeljak, H. Schäfer, D. Städter, M. Beyer, K. Biljakovic, and J. Demsar, Dynamics of Photoinduced Charge-Density-Wave to Metal Phase Transition in $\text{K}_{0.3}\text{MoO}_3$, *Phys. Rev. Lett.* **102**, 066404 (2009).
- [4] V. R. Morrison, R. P. Chatelain, K. L. Tiwari, A. Hendaoui, A. Bruhács, M. Chaker, and B. J. Siwick, A photoinduced metal-like phase of monoclinic VO_2 revealed by ultrafast electron diffraction, *Science* **346**, 445 (2014).
- [5] S. de Jong, R. Kukreja, C. Trabant, N. Pontius, C. Chang, T. Kachel, M. Beye, F. Sorgenfrei, C. Back, B. Bräuer *et al.*, Speed limit of the insulator-metal transition in magnetite, *Nat. Mater.* **12**, 882 (2013).
- [6] J. Liu, M. Kargarian, M. Kareev, B. Gray, P. J. Ryan, A. Cruz, N. Tahir, Y.-D. Chuang, J. Guo, J. M. Rondinelli *et al.*, Heterointerface engineered electronic and magnetic phases of NdNiO_3 thin films, *Nat. Commun.* **4**, 1 (2013).
- [7] S. Catalano, M. Gibert, V. Bisogni, O. Peil, F. He, R. Sutarto, M. Viret, P. Zubko, R. Scherwitzl, A. Georges *et al.*, Electronic transitions in strained SmNiO_3 thin films, *APL Mater.* **2**, 116110 (2014).
- [8] A. Maignan, F. Damay, C. Martin, and B. Raveau, Nickel-induced metal-insulator transition in the small a cation manganites $\text{Ln}_{0.5}\text{Ca}_{0.5}\text{MnO}_3$, *Mater. Res. Bull.* **32**, 965 (1997).
- [9] M. Melo Jorge, M. Nunes, R. Silva Maria, and D. Sousa, Metal-insulator transition induced by Ce doping in CaMnO_3 , *Chem. Mater.* **17**, 2069 (2005).
- [10] H. Yoshizawa, H. Kawano, Y. Tomioka, and Y. Tokura, Magnetic-field-induced metal-insulator transition in $\text{Pr}_{0.7}\text{Ca}_{0.3}\text{MnO}_3$, *J. Phys. Soc. Jpn.* **65**, 1043 (1996).
- [11] Y. Tomioka, A. Asamitsu, H. Kuwahara, Y. Moritomo, M. Kasai, R. Kumai, and Y. Tokura, Magnetic-field-induced metal-insulator transition in perovskite-type manganese oxides, *Phys. B: Condens. Matter* **237–238**, 6 (1997).
- [12] J. del Valle, Y. Kalcheim, J. Trastoy, A. Charnukha, D. N. Basov, and I. K. Schuller, Electrically Induced Multiple Metal-Insulator Transitions in Oxide Nanodevices, *Phys. Rev. Appl.* **8**, 054041 (2017).
- [13] J. Jeong, N. Aetukuri, T. Graf, T. D. Schladt, M. G. Samant, and S. S. Parkin, Suppression of metal-insulator transition in VO_2 by electric field-induced oxygen vacancy formation, *Science* **339**, 1402 (2013).
- [14] J. Zhang and R. D. Averitt, Dynamics and control in complex transition metal oxides, *Annu. Rev. Mater. Res.* **44**, 19 (2014).
- [15] E. Abreu, D. Meyers, V. K. Thorsmølle, J. Zhang, X. Liu, K. Geng, J. Chakhalian, and R. D. Averitt, Nucleation and growth bottleneck in the conductivity recovery dynamics of nickelate ultrathin films, *Nano Lett.* **20**, 7422 (2020).
- [16] V. A. Stoica, D. Puggioni, J. Zhang, R. Singla, G. L. Dakovski, G. Coslovich, M. H. Seaberg, M. Kareev, S. Middey, P. Kissin *et al.*, Magnetic order driven ultrafast phase transition in NdNiO_3 , *Phys. Rev. B* **106**, 165104 (2022).
- [17] S. Catalano, M. Gibert, V. Bisogni, F. He, R. Sutarto, M. Viret, P. Zubko, R. Scherwitzl, G. A. Sawatzky, T. Schmitt *et al.*, Tailoring the electronic transitions of NdNiO_3 films through (111)_{pc} oriented interfaces, *APL Mater.* **3**, 062506 (2015).
- [18] J. B. Torrance, P. Lacorre, A. I. Nazzal, E. J. Ansaldo, and C. Niedermayer, Systematic study of insulator-metal transitions in perovskites RNiO_3 ($R = \text{Pr, Nd, Sm, Eu}$) due to closing of charge-transfer gap, *Phys. Rev. B* **45**, 8209 (1992).
- [19] U. Staub, G. I. Meijer, F. Fauth, R. Allenspach, J. G. Bednorz, J. Karpinski, S. M. Kazakov, L. Paolasini, and F. d’Acapito, Direct Observation of Charge Order in an Epitaxial NdNiO_3 Film, *Phys. Rev. Lett.* **88**, 126402 (2002).
- [20] J. L. García-Muñoz, M. A. G. Aranda, J. A. Alonso, and M. J. Martínez-Lope, Structure and charge order in the anti-ferromagnetic band-insulating phase of NdNiO_3 , *Phys. Rev. B* **79**, 134432 (2009).
- [21] P. Ruello, B. Perrin, T. Pézeril, V. Gusev, S. Gougeon, N. Chigarev, P. Laffez, P. Picart, D. Mounier, and J. Breteau,

- Optoacoustical spectrum of the metal–insulator transition compound NdNiO₃: Sub-picosecond pump–probe study, *Phys. B: Condens. Matter* **363**, 43 (2005).
- [22] P. Ruello, S. Zhang, P. Laffez, B. Perrin, and V. Gusev, Ultrafast electronic dynamics in the metal–insulator transition compound NdNiO₃, *Phys. Rev. B* **76**, 165107 (2007).
- [23] P. Ruello, S. Zhang, P. Laffez, B. Perrin, and V. Gusev, Laser-induced coherent acoustical phonons mechanisms in the metal–insulator transition compound NdNiO₃: Thermal and nonthermal processes, *Phys. Rev. B* **79**, 094303 (2009).
- [24] V. Esposito, L. Rettig, E. M. Bothschafter, Y. Deng, C. Dornes, L. Huber, T. Huber, G. Ingold, Y. Inubushi, T. Katayama *et al.*, Dynamics of the photoinduced insulator-to-metal transition in a nickelate film, *Struct. Dyn.* **5**, 064501 (2018).
- [25] A. D. Caviglia, R. Scherwitzl, P. Popovich, W. Hu, H. Bromberger, R. Singla, M. Mitranio, M. C. Hoffmann, S. Kaiser, P. Zubko *et al.*, Ultrafast Strain Engineering in Complex Oxide Heterostructures, *Phys. Rev. Lett.* **108**, 136801 (2012).
- [26] A. D. Caviglia, M. Först, R. Scherwitzl, V. Khanna, H. Bromberger, R. Mankowsky, R. Singla, Y.-D. Chuang, W. S. Lee, O. Krupin, W. F. Schlotter, J. J. Turner, G. L. Dakovski, M. P. Minitti, J. Robinson, V. Scagnoli, S. B. Wilkins, S. A. Cavill, M. Gibert, S. Gariglio *et al.*, Photoinduced melting of magnetic order in the correlated electron insulator NdNiO₃, *Phys. Rev. B* **88**, 220401(R) (2013).
- [27] M. Först, A. Caviglia, R. Scherwitzl, R. Mankowsky, P. Zubko, V. Khanna, H. Bromberger, S. Wilkins, Y.-D. Chuang, W. Lee *et al.*, Spatially resolved ultrafast magnetic dynamics initiated at a complex oxide heterointerface, *Nat. Mater.* **14**, 883 (2015).
- [28] M. Först, K. R. Beyerlein, R. Mankowsky, W. Hu, G. Mattoni, S. Catalano, M. Gibert, O. Yefanov, J. N. Clark, A. Frano *et al.*, Multiple Supersonic Phase Fronts Launched at a Complex-Oxide Heterointerface, *Phys. Rev. Lett.* **118**, 027401 (2017).
- [29] B. Torriss, J. Margot, and M. Chaker, Metal–insulator transition of strained SmNiO₃ thin films: Structural, electrical and optical properties, *Sci. Rep.* **7**, 40915 (2017).
- [30] N. Shukla, T. Joshi, S. Dasgupta, P. Borisov, D. Lederman, and S. Datta, Electrically induced insulator to metal transition in epitaxial SmNiO₃ thin films, *Appl. Phys. Lett.* **105**, 012108 (2014).
- [31] See Supplemental Material at <http://link.aps.org/supplemental/10.1103/PhysRevMaterials.7.096201> for sample XRD and resistivity data, exponential fits, (002) Bragg peak FWHM, and integrated intensity trends for all fluences, half-order peak data, laser-induced heating calculation, thermal transport calculation, and Poisson expansion calculation, which includes Refs. [32–35,40].
- [32] M. K. Stewart, J. Liu, M. Kareev, J. Chakhalian, and D. N. Basov, Mott Physics Near the Insulator-to-Metal Transition in NdNiO₃, *Phys. Rev. Lett.* **107**, 176401 (2011).
- [33] V. Barbeta, R. Jardim, M. Torikachvili, M. Escote, F. Cordero, F. Pontes, and F. Trequattrini, Metal–insulator transition in Nd_{1-x}Eu_xNiO₃ probed by specific heat and anelastic measurements, *J. Appl. Phys.* **109**, 07E115 (2011).
- [34] J. Pérez-Cacho, J. Blasco, J. García, M. Castro, and J. Stankiewicz, Study of the phase transitions in SmNiO₃, *J. Phys.: Condens. Matter* **11**, 405 (1999).
- [35] M. Hooda and C. Yadav, Electronic properties and the nature of metal–insulator transition in NdNiO₃ prepared at ambient oxygen pressure, *Phys. B: Condens. Matter* **491**, 31 (2016).
- [36] M. H. Upton, Y. Choi, H. Park, J. Liu, D. Meyers, J. Chakhalian, S. Middey, J.-W. Kim, and P. J. Ryan, Novel Electronic Behavior Driving NdNiO₃ Metal–Insulator Transition, *Phys. Rev. Lett.* **115**, 036401 (2015).
- [37] I. C. Tung, P. V. Balachandran, J. Liu, B. A. Gray, E. A. Karapetrova, J. H. Lee, J. Chakhalian, M. J. Bedzyk, J. M. Rondinelli, and J. W. Freeland, Connecting bulk symmetry and orbital polarization in strained RNiO₃ ultrathin films, *Phys. Rev. B* **88**, 205112 (2013).
- [38] D. Walko, Y.-M. Sheu, M. Trigo, and D. Reis, Thermal transport in thin films measured by time-resolved, grazing incidence x-ray diffraction, *J. Appl. Phys.* **110**, 102203 (2011).
- [39] H. Wen, L. Guo, E. Barnes, J. H. Lee, D. A. Walko, R. D. Schaller, J. A. Moyer, R. Misra, Y. Li, E. M. Dufresne *et al.*, Structural and electronic recovery pathways of a photoexcited ultrathin VO₂ film, *Phys. Rev. B* **88**, 165424 (2013).
- [40] R. B. Wilson, B. A. Apgar, W.-P. Hsieh, L. W. Martin, and D. G. Cahill, Thermal conductance of strongly bonded metal–oxide interfaces, *Phys. Rev. B* **91**, 115414 (2015).
- [41] R. Li, O. A. Ashour, J. Chen, H. E. Elsayed-Ali, and P. M. Rentzepis, Femtosecond laser induced structural dynamics and melting of Cu (111) single crystal. An ultrafast time-resolved x-ray diffraction study, *J. Appl. Phys.* **121**, 055102 (2017).
- [42] B. Truc, P. Usai, F. Pennacchio, G. Berruto, R. Claude, I. Madan, V. Sala, T. LaGrange, G. M. Vanacore, S. Benhabib, and F. Carbone, Ultrafast generation of hidden phases via energy-tuned electronic photoexcitation in magnetite, [arXiv:2210.00070](https://arxiv.org/abs/2210.00070) [cond-mat.str-el] (2022).